

Mutual Inductance Calculation Method of Rectangular Coils with Bilateral Bounded Single-Hole Type Magnetic Medium in Wireless Power Transfer Systems

Lingjun Kong¹, Zhongbang Chen², Changxuan Hu², Chenxi Zhang²,
Jianbin Wang², Xin Zhou¹, Lin Jia², and Zhongqi Li^{1,2,3,*}

¹College of Electrical and Information Engineering, Hunan University of Technology, Zhuzhou 412007, China

²College of Railway Transportation, Hunan University of Technology, Zhuzhou 412007, China

³College of Electrical and Information Engineering, Hunan University, Changsha 410082, China

ABSTRACT: The mutual inductance between the transmitting and receiving coils is one of the critical parameters of the wireless power transfer system, and an accurate mutual inductance calculation method can provide a reliable theoretical basis for the optimization of the coil structure of the wireless power transfer system. The addition of magnetic medium materials on both sides of the rectangular coil can effectively increase the mutual inductance, but there is no study on the mutual inductance calculation method for a rectangular coil with a bilateral bounded single-hole type magnetic medium. In this paper, the space vector domain synthesis method is proposed to solve the analytical value of mutual inductance, which solves Poisson's and Laplace's equations by separating the variables to obtain the magnetic vector potential in each region, and combines with the magnetic field boundary conditions to obtain the mutual inductance calculation formula by utilizing different dimensional vector syntheses. An experimental set of wireless power transfer systems with bilateral bounded single-hole type magnetic medium rectangular coils is also constructed, and the maximum error of the mutual inductance calculation value, experimental value, and simulation value is 5.82%, which verifies the effectiveness of the method proposed in this paper. The model proposed in this paper saves 5.86% of the material compared with the rectangular magnetic medium structure under the same parameters, and the mutual inductance is up to 99% of the rectangular magnetic medium structure.

1. INTRODUCTION

Wireless Power Transfer (WPT) is a cutting-edge technology that utilizes electromagnetic waves and other media for energy transfer. Compared with the traditional electric energy transmission, the operation of wireless power transfer is more flexible, and the safety and reliability are also greatly improved. WPT technology is widely used in the fields of implantable medical devices [1], electric vehicle [2–6], unmanned aerial vehicle [7], underwater power supply methods [8], rail transportation [9], etc. A WPT system is mainly composed of two parts, transmitting coil and receiving coil, and in practice, the receiving coil will inevitably be horizontally offset, which will affect the mutual inductance between the coils. The calculation of mutual inductance between the coils can provide a theoretical basis for the optimization of the coil coupling structure; therefore, it is of great significance to study the method of calculating the mutual inductance between the transmitting coil and receiving coil.

Currently, common coil types in WPT systems include circular coils [10, 11] and rectangular coils. The calculation of mutual inductance between circular coils has been extensively studied, and these works are mainly based on the filament

method [12], completed elliptic integrals of type I and type II [13, 14], Bessel and Struve functions [15, 16], and Biot-Savart theorem [17].

Compared with circular coils, mutual inductance of rectangular coils is still less studied. For rectangular coils without magnetic medium, [18] gives an analytical method to calculate the mutual inductance between two coaxial planar helical rectangular coils based on second-order vector bits, but the horizontal offset is not discussed. Ref. [19] proposed a new method to model the mutual inductance using the coordinates of the coil vertices and solved the mutual inductance when the coil undergoes a horizontal offset. Ref. [20] numerically calculated the basic magnetic field equation generated by a DC charged conductor at any point in space based on the Biot-Savart theorem to derive a method for calculating the mutual inductance of two coils at an arbitrary position. None of the above literature incorporates a magnetic medium although various relative positions between rectangular coils are considered.

In order to improve the transmission efficiency of WPT systems, the incorporation of a magnetic medium into the magnetically coupled structure of a wireless power transmission system is usually considered. Ref. [21] incorporated a magnetic medium in a WPT system and derived a computational expression for the mutual inductance in a horizontally offset

* Corresponding author: Zhongqi Li (my3eee@126.com).

state based on the Fourier-Bessel transform and dyadic Fourier transform; however, this method only considers the thickness of the magnetic medium to be finite and does not take into account the boundedness of the length and width of the magnetic medium. Ref. [22] considered the variation of the width of the magnetic medium and obtained the mutual inductance calculation equation of the coil at arbitrary position by the expansion of Laplace's equation and hyperbolic function; however, the model constructed only considered the case of a single side of the magnetic medium. Refs. [23, 24] obtained the mutual inductance formulation for a bounded magnetic medium with two sides based on the superposition method of two 2D subdomain analytical models. The above literatures studied the case with a whole magnetic medium; however, none of them investigated the mutual inductance calculation method about when to save the magnetic medium material due to the high price of the material. In summary, the mutual inductance calculation of rectangular coils with bilateral bounded single-hole type dielectrics for wireless power transmission systems needs further study. Therefore, this paper establishes a three-dimensional model of a rectangular coil with bilateral bounded single-hole type dielectrics, as shown in Figure 1.

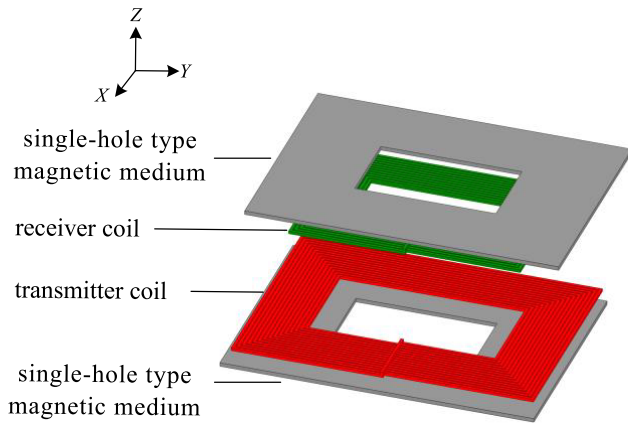


FIGURE 1. Three-dimensional view of rectangular coil with bilateral bounded single-hole type magnetic medium.

In this paper, the mutual inductance calculation formula of a rectangular coil with a bilateral bounded single-hole type magnetic medium is derived by the space vector domain synthesis method. Combined with finite element simulation and experimental measurements, the maximum error of mutual inductance between calculated, simulated, and experimental values is 5.82%, which verifies the validity of the method proposed in this paper, and the computation time required by the method proposed in this paper is shortened by at least 10 times compared with that of finite element analysis. Under the same parameters, the model proposed in this paper can save 5.86% of material compared with the moment-type dielectric structure, and the simulated value of mutual inductance can be up to 99% of the rectangular magnetic medium structure.

2. TWO-DIMENSIONAL MODELING OF RECTANGULAR COILS WITH BILATERAL BOUNDED SINGLE-HOLE TYPE MAGNETIC MEDIUM

In this paper, a two-dimensional x - z plane with a bilateral bounded single-hole type magnetic medium rectangular coil model is established as shown in Figure 2. In order to make the proposed method general, any two rectangular coils with different dimensions are taken for modeling and analysis. In this section, the coil system is divided into regions based on the material properties of the WPT system. In this case, regions $4b$ and $4d$ denote the cross-section of the transmitting coil, and copper wires are used for both the transmitting and receiving coils. Regions $2b$ and $2d$ and regions $6b$ and $6d$ are the magnetic medium on the transmitting and receiving coil sides, respectively, and the remaining portion is the air region.

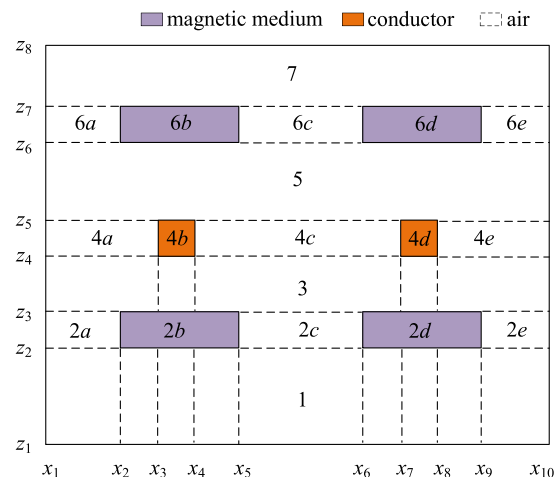


FIGURE 2. x - z plan of rectangular coil with bilateral bounded single-hole type medium.

2.1. Magnetic Vector Potential Expression for Each Region

The case of boundary coordinates of any region can be defined by dividing the two-dimensional x - z plane into regions, as shown in Figure 3 below. The start and end coordinates of region r on the x -axis are denoted by x_m and x_n , respectively, and similarly, it can be denoted by z_m and z_n on the z -axis. Then, x_m , x_n , z_m , and z_n of region $2c$ ($r = 2c$) are denoted by x_5 , x_6 , z_2 , and z_3 , respectively.

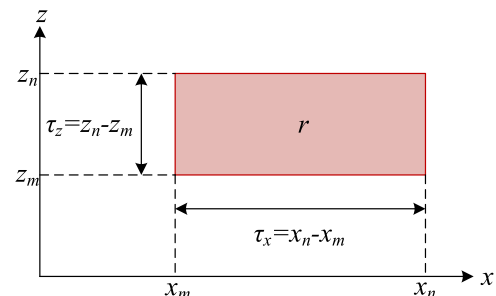


FIGURE 3. Schematic diagram of the x - z plane boundary coordinates of arbitrary region.

By solving Poisson's equation (1), the magnetic vector potential A_r can be obtained for regions 4b and 4d. It is worth noting that no current exists in the regions other than regions 4b and 4d, then the magnetic vector potential A_r satisfies Laplace's equation (2).

$$\frac{\partial^2 A_r}{\partial x^2} + \frac{\partial^2 A_r}{\partial z^2} = -\mu_0 \mu_r J_r \quad (1)$$

$$\frac{\partial^2 A_r}{\partial x^2} + \frac{\partial^2 A_r}{\partial z^2} = 0 \quad (2)$$

Separate variables are applied to the Poisson and Laplace equations to obtain the magnetic vector potential in each region A_r , where μ_0 is the magnetic permeability of the air medium, μ_r the relative magnetic permeability of the region r in which it is located, and J_r the current density induced by the emitting coil current I_p .

1) Regions 2b, 2d, 4b, 4d, 6b, and 6d

By solving Eq. (1), the magnetic vector potential flux solution for regions 4b and 4d where the transmitter coil is located can be obtained as shown in Eq. (3). By solving Eq. (2), the magnetic vector potential flux solution for 2b, 2d, 6b, and 6d regions where the magnetic medium is located can be obtained as shown in Eq. (4).

$$A_r = A_r^x + A_r^z + A_r^* \quad (3)$$

$$A_r = A_r^x + A_r^z \quad (4)$$

where A_r^x and A_r^z are the magnetic vector potential components obtained by applying boundary conditions on the x -side (i.e., x_m and x_n) and z -side (i.e., z_m and z_n), and A_r^* is the magnetic vector potential induced by the current density. The expressions for A_r^x , A_r^z , and A_r^* are given below:

$$A_r^x = (z_n - z) c_{0,r} + (z - z_m) d_{0,r} + \sum_{l_r=1}^{L_r} \cos(k_{x_r} (x - x_m)) \times \left(c_r \frac{\sinh(k_{x_r} (z_n - z))}{k_{x_r} \sinh(k_{x_r} \tau_{z_r})} + d_r \frac{\sinh(k_{x_r} (z - z_m))}{k_{x_r} \sinh(k_{x_r} \tau_{z_r})} \right) \quad (5)$$

$$A_r^z = \sum_{n_r=1}^{N_r} \sin(k_{z_r} (z - z_m)) \times \left(-e_r \frac{\cosh(k_{z_r} (x - x_n))}{k_{z_r} \sinh(k_{z_r} \tau_{x_r})} + f_r \frac{\cosh(k_{z_r} (x - x_m))}{k_{z_r} \sinh(k_{z_r} \tau_{x_r})} \right) \quad (6)$$

$$A_r^* = -0.5 \mu_0 J_r z^2 \quad (7)$$

Since there is no current in regions 2b, 2d, 6b, and 6d, the magnetic vector potential A_r^* induced by the current density is 0. In the above equations, $c_{0,r}$, $d_{0,r}$, c_r , d_r , e_r , f_r are all the coefficients to be solved; l_r , n_r are the numbers of spatial harmonics; and k_{x_r} , k_{z_r} are the spatial frequencies, which are given by the following expressions:

$$\begin{cases} k_{x_r} = l_r \pi / \tau_{x_r} \\ k_{z_r} = n_r \pi / \tau_{z_r} \end{cases} \quad (8)$$

2) Regions 2a, 2c, 2e, 4a, 4c, 4e, 6a, 6c, and 6e

Since these regions are air medium, according to Equation (2), the A_r^x and A_r^z expressions are obtained as follows:

$$A_r^x = \sum_{l_r=1}^{L_r} \sin(k_{x_r} (x - x_m)) \times \left(c_r \frac{\sinh(k_{x_r} (z_n - z))}{k_{x_r} \sinh(k_{x_r} \tau_{z_r})} + d_r \frac{\sinh(k_{x_r} (z - z_m))}{k_{x_r} \sinh(k_{x_r} \tau_{z_r})} \right) \quad (9)$$

$$A_r^z = \sum_{n_r=1}^{N_r} \sin(k_{z_r} (z - z_m)) \times \left(e_r \frac{\sinh(k_{z_r} (x - x_n))}{k_{z_r} \sinh(k_{z_r} \tau_{x_r})} + f_r \frac{\sinh(k_{z_r} (x - x_m))}{k_{z_r} \sinh(k_{z_r} \tau_{x_r})} \right) \quad (10)$$

As shown in Figure 2, the magnetic vector potential is zero to the left of the x -side (x_1) in regions 2a, 4a, and 6a, and zero to the right of the x -side (x_{10}) in regions 2e, 4e, and 6e. Therefore, e_r in regions 2a, 4a, and 6a is equal to zero, and f_r in regions 2e, 4e, and 6e is equal to zero.

3) Regions 1, 3, 5, and 7

Regions 1 and 7 are the bottom and top air regions of the constructed model, and regions 3 and 5 denote the air regions between the transmitting coil and magnetic dielectric material on both sides. Then, the magnetic vector potential expression is as follows:

$$A_r = A_r^x = \sum_{l_r=1}^{L_r} \sin(k_{x_r} (x - x_m)) \times \left(c_r \frac{\sinh(k_{x_r} (z_n - z))}{k_{x_r} \sinh(k_{x_r} \tau_{z_r})} + d_r \frac{\sinh(k_{x_r} (z - z_m))}{k_{x_r} \sinh(k_{x_r} \tau_{z_r})} \right) \quad (11)$$

It is worth noting that the magnetic vector potential on the lower side of the z -side (z_1) in region 1 is zero, so c_r in the magnetic vector potential of region 1 is zero. The magnetic vector potential on the upper side of the z -side (z_8) in region 7 is zero, so d_r in the magnetic vector potential of region 7 is also zero.

2.2. Boundary Conditions for 2D Models

According to the electromagnetic field boundary conditions: at the interfaces of different media, the magnetic vector potential A_r is continuous; the normal component of the magnetic flux density B_r and the tangential component of the magnetic field strength H_r are also continuous. The formulas for the magnetic flux density B_r and magnetic field strength H_r are as follows:

$$\begin{cases} B_r = \nabla \times A_r = \frac{\partial A_r}{\partial z} - \frac{\partial A_r}{\partial x} \\ H_r = \frac{B_r}{\mu_0 \mu_r} \end{cases} \quad (12)$$

Based on the division of regions in the previous subsection, all regions can be subdivided into cases as shown in Figures 4 and 5.

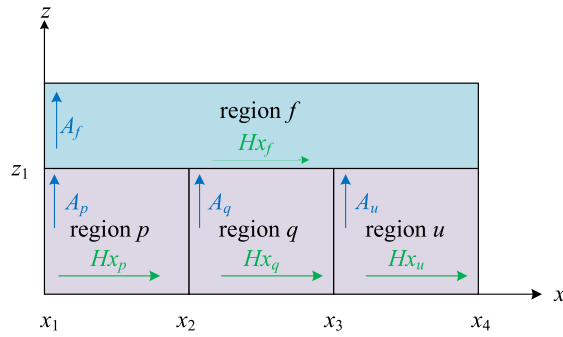


FIGURE 4. The tangential component of the magnetic field strength H_x and the magnetic vector potential A_x are continuous at z_1 .

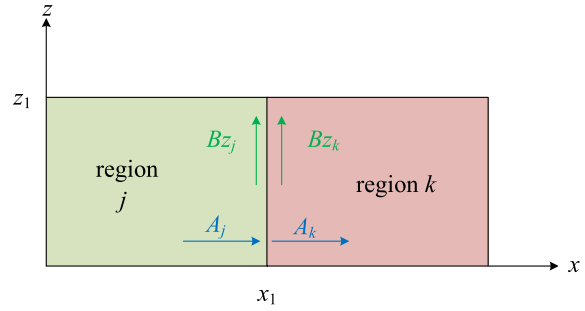


FIGURE 5. The magnetic vector potential A_x and the normal component of the magnetic flux density B_z are continuous at x_1 .

For the above case, the boundary conditions are shown in Equations (13)–(16) below:

$$A_f(x, z_1) = A_p(x_1, z_1) = A_q(x_2, z_1) = A_u(x_3, z_1) \quad (13)$$

$$H_{x_f}(x, z_1) = H_{x_p}(x_1, z_1) + H_{x_q}(x_2, z_1) + H_{x_u}(x_3, z_1) \quad (14)$$

$$A_j(x, z_1) = A_k(x, z_1) \quad (15)$$

$$B_{z_j}(x_1, z) = B_{z_k}(x_1, z) \quad (16)$$

2.3. Regional Coefficient Solution

Based on the discussion in the previous subsection, the boundary conditions corresponding to each region can be determined, followed by solving the linear equations to determine the unknown coefficients for each region. It may be useful to take region 3 as an example, which can be obtained by combining Figure 4 and Eq. (14):

$$H_{x_3}(x, z_3) = H_{x_{2a}}(x_{2a}, z_3) + H_{x_{2b}}(x_{2b}, z_3) + H_{x_{2c}}(x_{2c}, z_3) + H_{x_{2d}}(x_{2d}, z_3) + H_{x_{2e}}(x_{2e}, z_3) \quad (17)$$

Expanding Eq. (17) through the Fourier series yields the following expression for the unknown coefficients in region 3:

$$c_3 = \frac{2\mu_0\mu_3}{\tau_{x_3}} \left(\int_{x_1}^{x_2} H_{x_{2a}}(x_{2a}, z_3) dx + \int_{x_2}^{x_5} H_{x_{2b}}(x_{2b}, z_3) dx + \int_{x_5}^{x_6} H_{x_{2c}}(x_{2c}, z_3) dx + \int_{x_6}^{x_9} H_{x_{2d}}(x_{2d}, z_3) dx + \int_{x_9}^{x_{10}} H_{x_{2e}}(x_{2e}, z_3) dx \right) \sin(k_{x_3}(x - x_1)) dx \quad (18)$$

where $x_{2a} = x_2 - x_1$, $x_{2b} = x_5 - x_2$, $x_{2c} = x_6 - x_5$, $x_{2d} = x_9 - x_6$, and $x_{2e} = x_{10} - x_9$. For the other regions, the above method can be repeated with reference to region 3, yielding the matrix form as follows:

$$[T] \cdot [S] = [I] \quad (19)$$

In Eq. (19), $[T]$ represents the system boundary condition matrix. $[S]$ is the coefficient matrix, and the coefficients to be solved inside the coefficient matrix are sequentially arranged in the order of regions, as shown in Eq. (20). $[I]$ is the excitation source matrix, which is specifically expressed as Eq. (25),

where $[I_1], \dots, [I_7]$ denote the excitation current matrices of each region.

$$[S] = [[S_1] [S_{2a}] [S_{2b}] \dots [S_{6e}] [S_7]]^T \quad (20)$$

Each element in $[S]$ is a submatrix representing the unknown coefficients in the magnetic vector potential, as shown in Eqs. (21)–(24) below:

$$[S_1 \ S_3 \ S_5 \ S_7] = [d_1 \ c_3 \ d_3 \ c_5 \ d_5 \ c_7] \quad (21)$$

$$[S_{2a} \ S_{2b} \ S_{2c} \ S_{2d} \ S_{2e}] = \begin{bmatrix} c_{2a} & d_{2a} & f_{2a} & c_{0_{2b}} & c_{2b} & d_{0_{2b}} & d_{2b} \\ e_{2b} & f_{2b} & c_{2c} & d_{2c} & e_{2c} & f_{2c} & c_{0_{2d}} & c_{2d} \\ d_{0_{2d}} & d_{2d} & e_{2d} & f_{2d} & c_{2e} & d_{2e} & e_{2e} \end{bmatrix} \quad (22)$$

$$[S_{4a} \ S_{4b} \ S_{4c} \ S_{4d} \ S_{4e}] = \begin{bmatrix} c_{4a} & d_{4a} & f_{4a} & c_{0_{4b}} & c_{4b} & d_{0_{4b}} & d_{4b} \\ e_{4b} & f_{4b} & c_{4c} & d_{4c} & e_{4c} & f_{4c} & c_{0_{4d}} & c_{4d} \\ d_{0_{4d}} & d_{4d} & e_{4d} & f_{4d} & c_{4e} & d_{4e} & e_{4e} \end{bmatrix} \quad (23)$$

$$[S_{6a} \ S_{6b} \ S_{6c} \ S_{6d} \ S_{6e}] = \begin{bmatrix} c_{6a} & d_{6a} & f_{6a} & c_{0_{6b}} & c_{6b} & d_{0_{6b}} & d_{6b} \\ e_{6b} & f_{6b} & c_{6c} & d_{6c} & e_{6c} & f_{6c} & c_{0_{6d}} & c_{6d} \\ d_{0_{6d}} & d_{6d} & e_{6d} & f_{6d} & c_{6e} & d_{6e} & e_{6e} \end{bmatrix} \quad (24)$$

$$[I] = [[I_1] [I_{2a}] [I_{2b}] \dots [I_{6e}] [I_7]]^T \quad (25)$$

Simplifying Eq. (18) to Eq. (26), and the same for the rest of the region, the matrix $[T]$ can be expressed as Eq. (27), where $[E]$ is the unit matrix.

$$c_3 = [T_3^{2a}] + [T_3^{2b}] + [T_3^{2c}] + [T_3^{2d}] + [T_3^{2e}] \quad (26)$$

3. COMPUTATION OF MUTUAL INDUCTANCE OF 3D RECTANGULAR COILS WITH DIFFERENT DIMENSIONAL VECTOR SYNTHESIS

3.1. Three-Dimensional Correction Function

Since the two-dimensional model has an infinite length in the third direction, this is not the case for the actual coil system. In order to solve this problem, the length of the third direction needs to be finite, at which time a correction factor should be introduced. Based on the Biot-Savart theorem and the ratio of the flux density excited by an infinite-length wire to that excited by a finite-length wire, the correction coefficient for two

where $B_5(x, z)$ is the two-dimensional model flux density in the x - z plane, and $B_5(y, z)$ is the two-dimensional model flux density in the y - z plane. The expression is as follows:

$$B_5(x, z) = \frac{\partial A_5}{\partial z} \cdot f_{xz}(x, y, z, \mu_r) \quad (36)$$

$$B_5(y, z) = -\frac{\partial A_5}{\partial x} \cdot f_{yz}(x, y, z, \mu_r) \quad (37)$$

Finally, the computational expression for the mutual inductance of the rectangular coil with bilateral bounded single-hole type magnetic medium proposed in this paper is given by:

$$M = \frac{1}{I_p} \sum_{t=1}^{N_s} \left(\int_{x_3+t \cdot w}^{x_8-t \cdot w} \int_{y_3+t \cdot w}^{y_8-t \cdot w} B_5(x, y, z) dx dy \right) \quad (38)$$

where N_s is the number of turns of the receiving coil, and w is the diameter of the receiving coil. Figure 7 is a specific flowchart for the mutual inductance calculation of a rectangular coil with a bilateral bounded single-hole type magnetic medium.

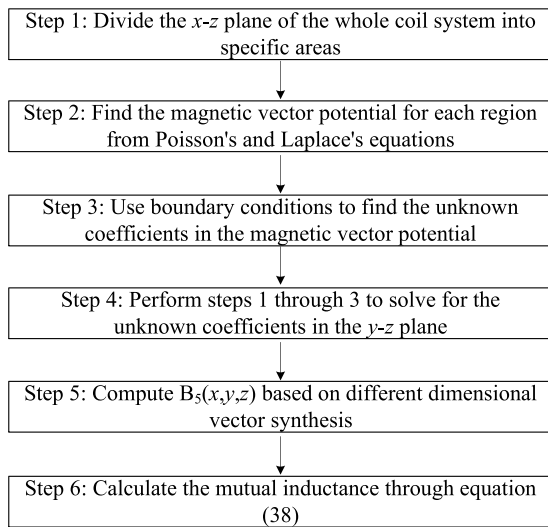


FIGURE 7. Flow chart of mutual inductance calculation.

4. SIMULATION AND EXPERIMENTAL VERIFICATION

In order to verify the correctness of the proposed mutual inductance calculation formula, Maxwell Ansys software modeling is used for simulation verification in this paper. At the same time, an experimental setup of a wireless energy transmission system with bilateral single-hole type magnetic dielectric rectangular coils is also constructed, as shown in Figure 8. The relative position change between the coils is realized by operating the 3D motion platform, the experimental value of mutual inductance measured by using the impedance analyzer IM3536, and the current frequency set to 85 kHz. The specific parameters of the coil system and magnetic dielectric material are shown in Table 1, and the coordinate parameter settings of the constructed 3D model are shown in Table 2.

TABLE 1. Parameter values.

Parameter	Value
Receiving and transmitting coil diameter/mm	5
Transmitter coil turns	15
Receiving coil turns	12
Relative permeability of a magnetic medium	2800
Thickness of single-hole type magnetic medium/mm	5
Transmitter coil current/A	10
Harmonic number (N_1, N_3, N_5, N_7)	2100
Harmonic number ($N_{2a}, N_{2b}, N_{2c}, N_{2d}, N_{2e}, L_{2a}, L_{2b}, L_{2c}, L_{2d}, L_{2e}$)	30
Harmonic number (N_{4a}, N_{4c}, N_{4e})	21
Harmonic number ($N_{4b}, N_{4d}, L_{4a}, L_{4b}, L_{4c}, L_{4d}, L_{4e}$)	30
Harmonic number ($N_{6a}, N_{6b}, N_{6c}, N_{6d}, N_{6e}, L_{6a}, L_{6b}, L_{6c}, L_{6d}, L_{6e}$)	30

TABLE 2. Geometric parameters.

x -direction/mm	y -direction/mm	z -direction/mm
$x_1 = 0$	$y_1 = 0$	$z_1 = -1015.09$
$x_2 = 1000$	$y_2 = 1000$	$z_2 = -15.09$
$x_3 = 1008.23$	$y_3 = 1003.23$	$z_3 = -10.09$
$x_4 = 1081.77$	$y_4 = 1076.77$	$z_4 = -5$
$x_5 = 1120$	$y_5 = 1115$	$z_5 = 0$
$x_6 = 1160$	$y_6 = 1275$	$z_6 = 20.09$
$x_7 = 1198.23$	$y_7 = 1313.23$	$z_7 = 25.09$
$x_8 = 1271.77$	$y_8 = 1386.77$	$z_8 = 1025.09$
$x_9 = 1280$	$y_9 = 1390$	/
$x_{10} = 2280$	$y_{10} = 2390$	/

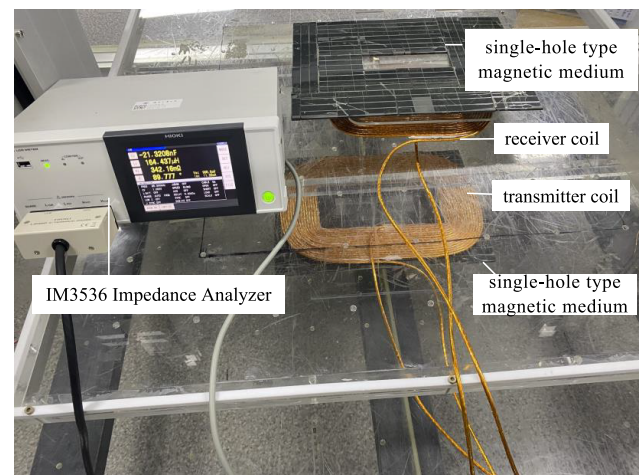


FIGURE 8. Diagram of the experimental setup.

$L_{eq1} = L_1 + L_2 + 2M$ when the receiving and transmitting coils are in series in the same direction, and $L_{eq1} = L_1 + L_2 - 2M$ when the receiving and transmitting coils are in series in the reverse directions, where L_1 and L_2 denote the self-inductance of the transmitting and receiving coils, respectively. The mutual inductance $M = \frac{1}{4} |L_{eq1} - L_{eq2}|$ between the two coils is measured by measuring the inductance L_{eq1} when the transmitting and receiving coils are connected in series in the same direction and L_{eq2} when they are connected in series in the

reverse directions. The coil mutual inductance test connection diagram is shown in Figure 9.

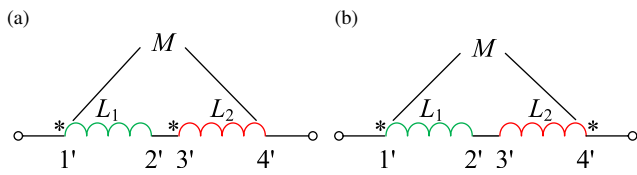


FIGURE 9. Connection diagram of coil mutual inductance experiment. (a) Coaxial series. (b) Inverted series.

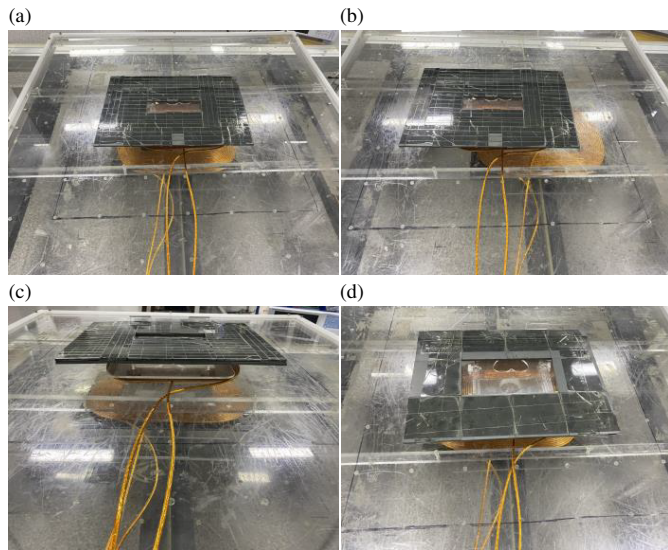


FIGURE 10. Experimental model of relative position of coils. (a) Vertical offset. (b) Horizontal offsets. (c) Changing the thickness of the magnetic medium. (d) Changing the size of the magnetic media cutout.

The experiments were verified from four cases of horizontal offset, vertical offset, changing the size of the magnetic medium skeleton and changing the thickness of the magnetic medium, and the experimental model is shown in Figure 10. ϵ_1 denotes the computational error, and ϵ_2 denotes the experimental error, and the two expressions are as follows:

$$\epsilon_1 = \frac{|M_c - M_s|}{M_c} \times 100\% \quad (39)$$

$$\epsilon_2 = \frac{|M_c - M_e|}{M_c} \times 100\% \quad (40)$$

where M_c is the calculated value of mutual inductance, M_s the simulated value of mutual inductance, and M_e the experimental value of mutual inductance. All subsequent errors in this paper are defined as above.

4.1. Horizontal Offset

The horizontal offset of the receiving coil occurs as shown in Figure 11, and Δx represents the horizontal offset distance of the receiving coil along the positive direction of the X -axis. The vertical distance between the two coils is set to $zz = 60$ mm, and the results and errors of the mutual inductance calculated, simulated, and experimental values are shown

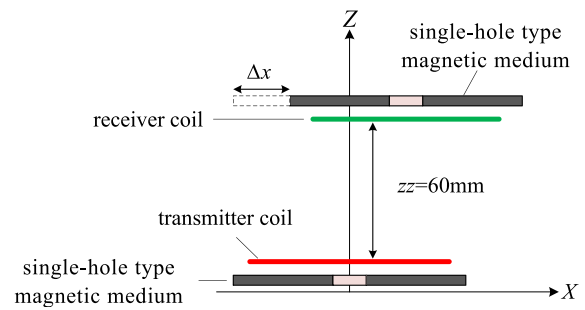


FIGURE 11. Schematic diagram of horizontal offset.

TABLE 3. Mutual inductance and error at horizontal offset.

$\Delta x/\text{mm}$	$M_c/\mu\text{H}$	$M_s/\mu\text{H}$	$M_e/\mu\text{H}$	ϵ_1 (%)	ϵ_2 (%)
-50	36.120	35.785	35.674	0.93	1.23
-40	39.527	38.825	38.454	1.78	2.71
-30	42.410	41.456	42.220	2.25	0.45
-20	44.600	43.575	44.121	2.30	1.07
-10	46.001	44.838	45.523	2.53	1.04
0	46.276	45.274	46.894	2.17	1.34
10	46.070	44.834	45.265	2.68	1.75
20	44.738	43.520	44.367	2.72	0.83
30	42.592	41.479	42.228	2.61	0.85
40	39.774	38.809	39.133	2.43	1.61
50	36.473	35.747	35.995	1.99	1.31

in Table 3 for the process of the receiving coil being uniformly offset from $\Delta x = -50$ mm to $+50$ mm in steps of 10 mm.

By analyzing the experimental data in Table 3, it can be seen that the mutual inductance calculation error ϵ_1 is not greater than 2.72%, and the experimental error ϵ_2 is not greater than 2.71% during the offset of the receiving coil from $\Delta x = -50$ mm to $+50$ mm. It is proved that the calculated, simulated, and experimental values of mutual inductance are in good agreement. According to the data in Table 3, the mutual inductance curve at horizontal offset is plotted, as shown in Figure 12.

Observation of Figure 12 shows that the mutual inductance value reaches its maximum when the vertical distance between

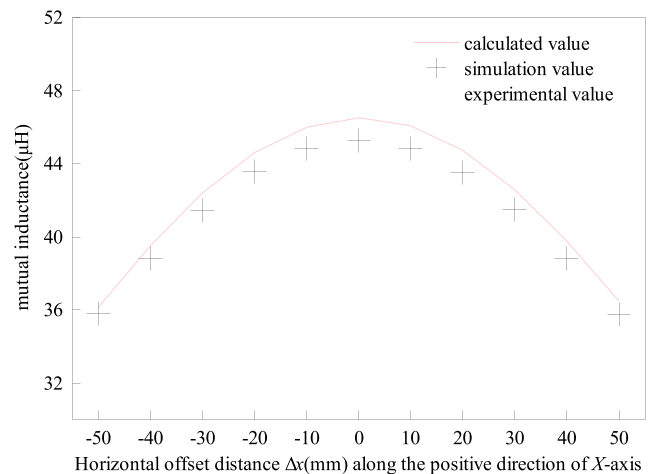


FIGURE 12. Mutual inductance graph at horizontal offset.

the transmitting coil and receiving coil is kept constant at 60 mm and when no horizontal offset occurs between the two coils. As the horizontal offset distance increases, the mutual inductance value decreases accordingly. This is because the larger the horizontal offset distance is, the smaller the overlap area of the magnetic field distribution is between the two coils, resulting in a decrease in the mutual inductance value.

4.2. Vertical Offset

The transmitting coil keeps the initial position unchanged, and the receiving coil is offset along the positive direction of the Z-axis. The position change of the vertical offset is shown in Figure 13. The initial vertical distance between the two coils $z = 10$ mm, and the vertical offset distance Δz is shifted in steps of 10 mm to 100 mm. The results and errors of the mutual inductance calculated, simulated, and experimental values are shown in Table 4.

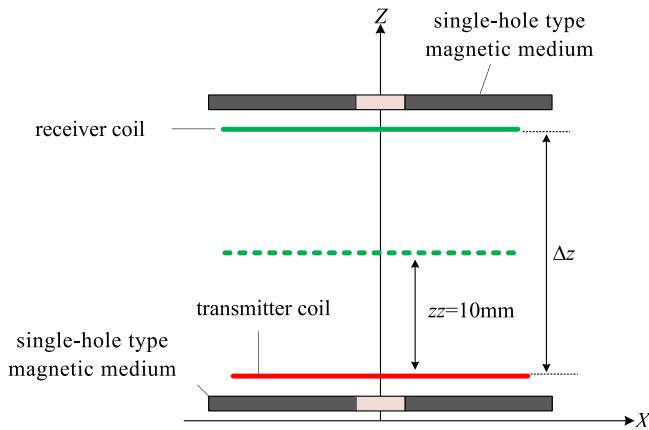


FIGURE 13. Schematic diagram of vertical offset.

TABLE 4. Experimental results.

Δz /mm	$M_c/\mu\text{H}$	$M_s/\mu\text{H}$	$M_e/\mu\text{H}$	ϵ_1 (%)	ϵ_2 (%)
10	124.283	131.400	124.870	5.73	0.47
20	98.013	101.140	98.547	3.19	0.54
30	79.165	80.058	81.234	1.13	2.61
40	65.580	65.321	65.338	0.39	0.37
50	54.912	53.565	55.116	2.45	0.37
60	46.276	45.274	47.894	2.17	3.50
70	39.155	39.298	39.469	0.37	0.80
80	33.208	33.832	33.543	1.88	1.01
90	28.368	29.300	28.775	3.29	1.43
100	24.132	25.536	25.241	5.82	4.60

Analyzing the data in Table 4, it can be seen that when the vertical distance between the transmitting coil and receiving coil is within 10–100 mm, the mutual inductance calculation error ϵ_1 is not greater than 5.82%, and the experimental error ϵ_2 is not greater than 4.60%. The calculated, experimental, and simulated values of mutual inductance are in good agreement. According to the data in Table 4, the mutual inductance curves of the calculated, simulated, and experimental values of mutual inductance at vertical offset are plotted, as shown in Figure 14.

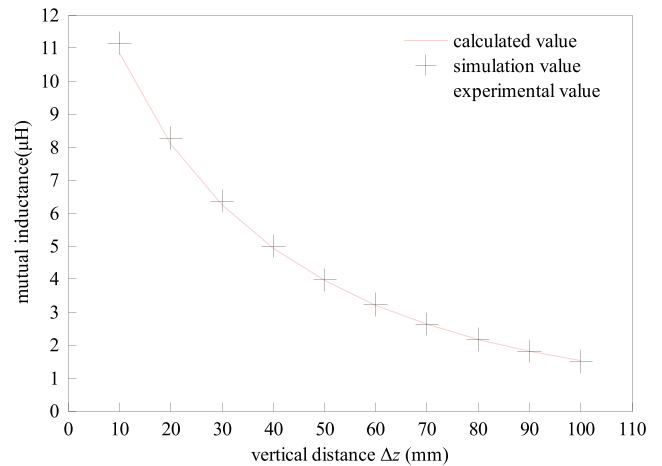


FIGURE 14. Mutual inductance graph at vertical offset.

The observation of Figure 14 shows that the mutual inductance value decreases nonlinearly as the perpendicular distance between the two coils increases because the magnetic flux between the interspersed two coils decreases as the perpendicular distance increases, and the tendency of the flux to decrease does not vary linearly with the perpendicular distance.

4.3. Changing the Size of the Magnetic Medium Cutout

The vertical distance between the two coils is set to $z = 30$ mm. Firstly, the width of the skeletonized part of the magnetic medium is kept constant at 160 mm, and the length of the skeletonized part is increased from 20 mm to 60 mm, as shown in Figure 15. Then, the length of the skeletonized part is kept constant at 40 mm, and the width of the skeletonized part is increased from 140 mm to 180 mm, as shown in Figure 16. The results and errors of the calculated, simulated, and experimental values of mutual inductance are shown in Tables 5 and 6.

TABLE 5. Mutual inductance and error when changing the skeleton length of magnetic medium.

x	$M_c/\mu\text{H}$	$M_s/\mu\text{H}$	$M_e/\mu\text{H}$	ϵ_1 (%)	ϵ_2 (%)
20	83.172	80.831	81.453	2.81	2.07
30	81.560	79.768	80.447	2.20	1.36
40	79.638	78.536	79.653	1.38	0.02
50	77.581	76.893	78.552	0.89	1.25
60	75.519	75.161	76.871	0.47	1.79

TABLE 6. Mutual inductance and error when changing the skeleton width of the magnetic medium.

y	$M_c/\mu\text{H}$	$M_s/\mu\text{H}$	$M_e/\mu\text{H}$	ϵ_1 (%)	ϵ_2 (%)
140	80.549	78.928	78.524	2.01	2.51
150	80.018	78.784	79.336	1.54	0.85
160	79.638	78.536	79.653	1.38	0.02
170	79.294	78.327	77.256	1.22	2.57
180	78.956	77.952	78.116	1.27	1.06

Analyzing the data in Table 5 and Table 6, it can be seen that when the vertical distance between the transmitting coil and receiving coil is 30 mm; the width of the skeletonized part

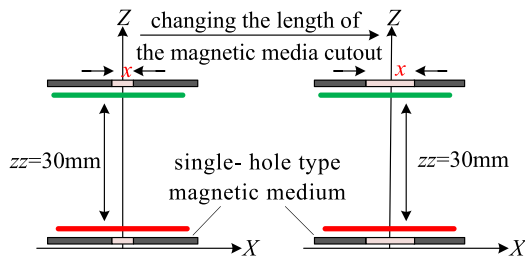


FIGURE 15. Changing the length of the hollowed-out portion of the magnetic medium.

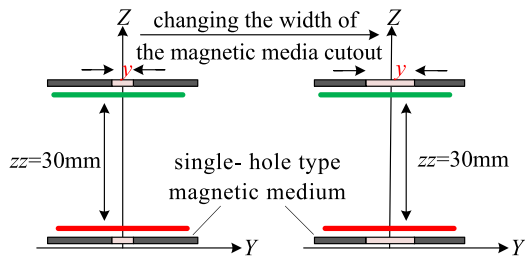


FIGURE 16. Changing the width of the hollowed-out portion of the magnetic medium.

of the magnetic medium remains unchanged; and the length of the skeletonized part is increased from 20 mm to 60 mm, the computational error ε_1 is not greater than 2.81%, and the experimental error ε_2 is not greater than 2.07%. When the length of the skeletonized part of the magnetic medium remains unchanged; the width of the skeletonized part is increased from that when the length of the skeletonized part of the magnetic medium remains unchanged; and the width of the skeletonized part is increased from 140 mm to 180 mm, the calculation error ε_1 is not greater than 2.01%, and the experimental error ε_2 is not greater than 2.51%. It is proved that the calculated, simulated, and experimental values of mutual inductance still maintain good consistency when the skeleton size of the magnetic medium is changed. Combined with the data in Table 5 and Table 6, the mutual inductance curves are plotted for different magnetic medium skeleton sizes, as shown in Figures 17 and 18.

Analyzing Figures 17 and 18 shows that as the length of the skeletonized portion of the magnetic medium is kept constant, the value of mutual inductance decreases when the width of the skeletonized portion increases, and increases when the width of the skeletonized portion decreases. Similarly, the same result is obtained by changing the length of the skeletonized portion of the magnetic medium while keeping the width of the skeletonized portion of the magnetic medium constant. This is due to the negative correlation between the magnetic leakage and the area of the skeletonized part of the magnetic medium, and the smaller the area of the skeletonized part is, the smaller the magnetic leakage is, and the larger the mutual inductance value is.

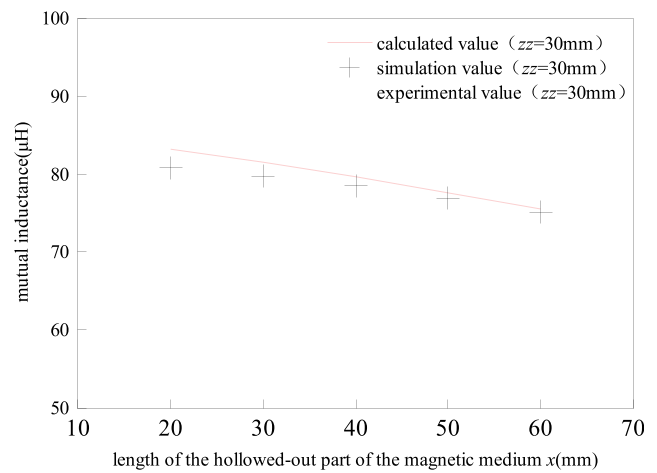


FIGURE 17. Plot of mutual inductance when changing the width of the openwork portion of the magnetic medium.

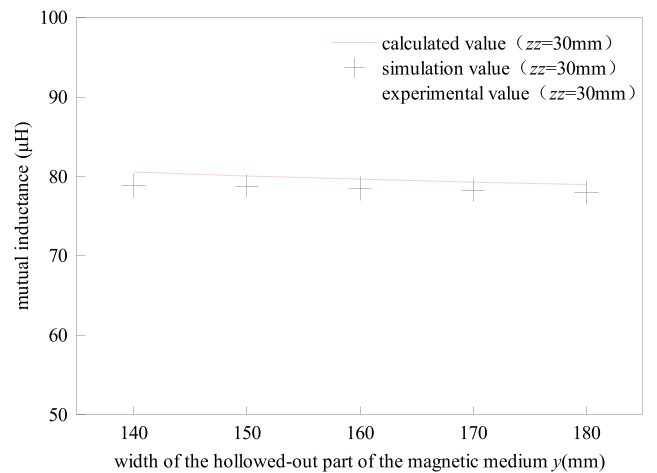


FIGURE 18. Plot of mutual inductance variation when changing the length of the hollowed-out portion of the magnetic medium.

4.4. Changing the Thickness of the Magnetic Medium

In this subsection, in order to verify that the proposed method is still effective when the thickness of the magnetic medium is changed, five sets of different thicknesses of the magnetic

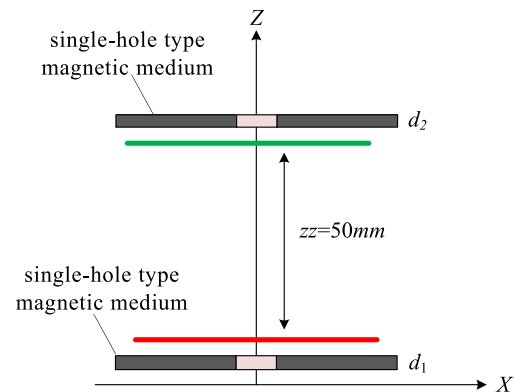


FIGURE 19. Schematic diagram of different magnetic medium thickness.

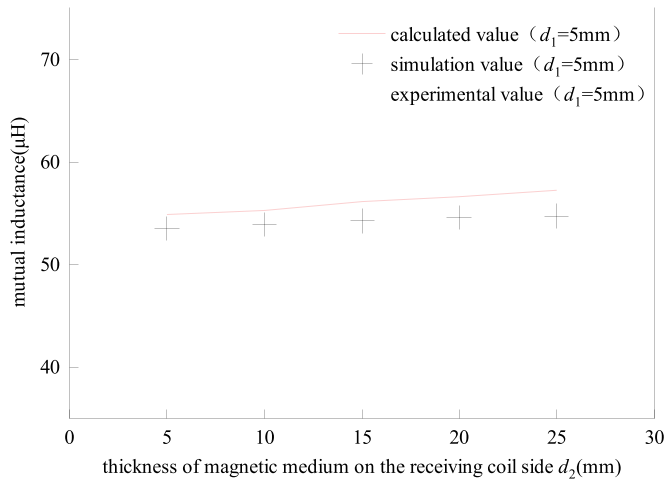


FIGURE 20. Mutual inductance curves for magnetic medium thickness $d_1 = 5$ mm on the transmitter side.

TABLE 7. Mutual inductance and error at different thickness of magnetic medium.

d_1	d_2	$M_c/\mu\text{H}$	$M_s/\mu\text{H}$	$M_e/\mu\text{H}$	ε_1 (%)	ε_2 (%)
5	5	54.912	53.510	54.125	2.55	1.43
5	10	55.289	53.970	54.654	2.39	1.15
5	15	56.134	54.288	55.268	3.29	1.54
5	20	56.599	54.534	55.414	3.65	2.09
5	25	57.251	54.762	57.031	4.35	0.38
10	5	55.328	54.065	54.121	2.28	2.18
10	10	55.810	54.588	54.025	2.19	3.20
10	15	56.664	54.938	55.776	3.05	1.57
10	20	57.166	55.097	55.784	3.62	2.42
10	25	57.806	55.332	56.523	4.28	2.22

medium are selected when the vertical distance between the coils is 50 mm, and the thicknesses of the magnetic medium on the transmitting coil side and receiving coil side are denoted by d_1 and d_2 , respectively, as shown in Figure 19. Combining the mutual inductance calculated values, simulated values, and experimental values, the mutual inductance data under different thicknesses of magnetic medium are obtained as shown in Table 7.

Table 7 shows that the computational error ε_1 is not greater than 4.35%, and the experimental error ε_2 is not greater than 3.20%. The calculated, simulated and experimental values of mutual inductance are in good agreement. Combined with the data in Table 7, the mutual inductance curves are plotted for different thicknesses of magnetic medium, as shown in Figures 20 and 21.

The observation of Figures 20 and 21 shows that as the thickness of the magnetic medium increases, the mutual inductance between the two coils increases accordingly, which is because the increase in the thickness of the magnetic medium can

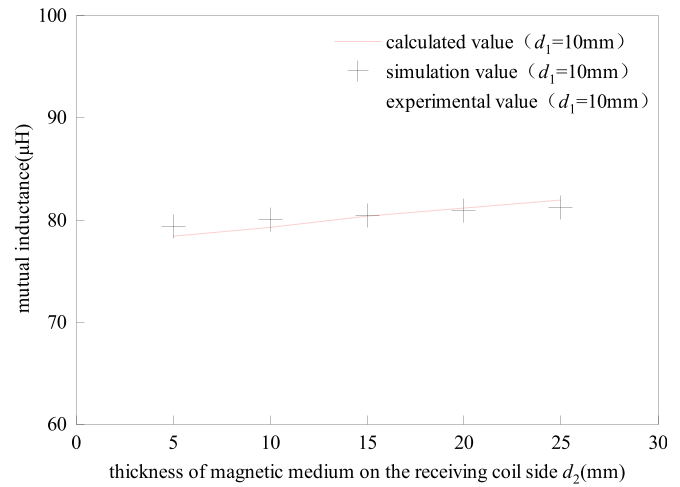


FIGURE 21. Mutual inductance curves for magnetic medium thickness $d_1 = 10$ mm on the transmitter side.

weaken the magnetic field. However, the effect of the thickness of the magnetic medium does not play a critical role, resulting in a small change in the mutual inductance.

4.5. Comparison

In this section, the computational method proposed in this paper is compared with the running time of Ansys Maxwell simulation software, as shown in Table 8, where t_a denotes the average time required by the method proposed in this paper, and t_b denotes the average time required by the Ansys Maxwell simulation. Case₁ denotes the case when the receiving coil is horizontally offset; Case₂ denotes the case when the receiving coil is vertically offset; Case₃ denotes the case when the size of the magnetic dielectric skeletonization is changed; Case₄ denotes the case when the thickness of the magnetic medium is changed.

TABLE 8. Comparison of running times for different cases.

	Case ₁	Case ₂	Case ₃	Case ₄
t_a/s	12.3	10.2	11.4	11.2
t_b/s	224.5	240.8	112.5	160.3

TABLE 9. Mutual inductance simulation value of single-hole type and rectangular magnetic medium at horizontal offset.

x/mm	$M_1/\mu\text{H}$	$M_2/\mu\text{H}$	γ (%)
-50	35.785	36.147	99.00
-40	38.825	39.438	98.45
-30	41.456	42.153	98.35
-20	43.575	44.166	98.66
-10	44.838	45.402	98.76
0	45.274	45.795	98.86
10	44.834	45.333	98.90
20	43.520	44.139	98.60
30	41.479	42.113	98.49
40	38.809	39.370	98.58
50	35.747	36.107	99.00

TABLE 10. Comparison of mutual inductance calculation methods at domestic and abroad.

Literatures	Methodologies	VO	HO	UMM	BMM	FMM	SM
[18]	Second-order vector bits	✓	×	×	×	×	×
[19]	Vertex coordinate method	✓	✓	×	×	×	×
[20]	Biot-Saval theorem	✓	✓	×	×	×	×
[21]	Fourier transform	✓	✓	✓	×	×	×
[22]	Split-variable method	✓	✓	✓	×	✓	×
[23]	Subdomain superposition method	✓	✓	✓	✓	✓	×
[24]	Subdomain superposition method	✓	✓	✓	✓	✓	×
This work	Space vector domain synthesis method	✓	✓	✓	✓	✓	✓

Table 8 shows that under the same computer configuration (CPU: i9-13900KF, RAM: 64 GB), the proposed method takes only 10.2 s for the shortest running time and 12.3 s for the longest running time in the above cases, while the Ansys Maxwell simulation time is 112.5 s for the shortest running time and 240.8 s for the longest running time, so that the computational time needed by the proposed method in this paper is at least 10 times shorter than that by the finite element analysis. The method proposed in this paper requires at least 10 times shorter computation time than the finite element analysis. In conclusion, the rapidity and superiority of the proposed method are verified.

In the model proposed in this paper, the ring-type magnetic medium has a 40 mm × 160 mm skeleton, which saves 5.86% of material compared with the rectangular-type magnetic medium. As the area of the dielectric skeletonized portion of the single-hole type increases, the material saving rate increases accordingly. In order to further compare the change of mutual inductance before and after the material saving, the simulated values of mutual inductance between the two in the horizontal offset state are analyzed at a vertical offset distance of 60 mm, as shown in Table 9.

M_1 and M_2 in the table denote the simulated values of mutual inductance for ring-type and moment-type magnetic medium, respectively, and γ denotes the ratio between M_1 and M_2 .

Analysis of the data in Table 9 shows that the simulated value of mutual inductance for the rectangular coil model with bilateral single-hole type dielectric is 99% of the simulated value of mutual inductance for the rectangular dielectric structure.

Table 10 shows the comparison between the calculation method proposed in this paper and the work of others. In the table, VO denotes the vertical offset; HO denotes horizontal offset; UMM denotes the unilateral magnetic medium; BMM denotes the bilateral magnetic medium; FMM denotes the bounded magnetic medium; and SM denotes the saving materials. Observing Table 10, it can be seen that compared with [18–22], the calculation method proposed in this paper realizes a bilateral bounded magnetic medium while considering the horizontal offset of the receiving coil. Moreover, this paper is superior to [23, 24] in calculating the mutual inductance of a rectangular coil with bilateral bounded magnetic medium by considering the material saving of the magnetic medium.

5. CONCLUSION

In this paper, a three-dimensional model of a rectangular coil with bilateral bounded single-hole type magnetic medium for wireless energy transmission system is established, and the space vector domain synthesis method is proposed to solve the analytical value of mutual inductance. The method obtains the magnetic vector potential of each region by solving Poisson's and Laplace's equations by separating the variables, and the mutual inductance calculation formula is obtained by using different dimensional vector syntheses in combination with the magnetic field boundary conditions. The maximum error of mutual inductance calculation value, experimental value, and simulation value is 5.82%, which verifies the effectiveness of the calculation method proposed in this paper. Meanwhile, the model proposed in this paper saves 5.86% of material compared with the moment-type dielectric structure under the same parameters, and the mutual inductance can be up to 99% of the moment-type dielectric structure. The calculation method provided in this paper can provide a theoretical basis for the optimization of the coil structure of the wireless power transmission system, and it has certain reference significance for the next step of the mutual inductance calculation method of rectangular coils with convex single-hole type dielectrics.

ACKNOWLEDGEMENT

This work was supported in part by the Natural Science Foundation of Hunan Province under Grants 2022JJ30226, National Key R&D Program Project (2022YFB3403200), Key Projects of Hunan Provincial Department of Education (23A0432), Outstanding Youth Project of Scientific Research Program of Hunan Provincial Department of Education (22B0577) and National Natural Science Foundation of China Youth Science Fund Project (62303178).

REFERENCES

- [1] Chen, W., J. Song, and X. Yan, "Wireless power supply voltage regulation control of implantable devices based on primary side MPC," *Progress In Electromagnetics Research C*, Vol. 122, 183–198, 2022.
- [2] Zhang, X., L. Ren, P. Kong, X. Xiong, and Z. Li, "Study of a double-layer passive magnetic shielding system for electric ve-

- hicle WPT,” *Progress In Electromagnetics Research C*, Vol. 137, 65–79, 2023.
- [3] Mou, W. and M. Lu, “Research on shielding and electromagnetic exposure safety of an electric vehicle wireless charging coil,” *Progress In Electromagnetics Research C*, Vol. 117, 55–72, 2021.
- [4] Liu, S., D. Li, C. Chen, W. Jia, K. Che, and J. Yu, “Electromagnetic field safety analysis of a 7.7 kW wireless power transfer system for electric vehicles,” *Progress In Electromagnetics Research M*, Vol. 117, 1–12, 2023.
- [5] Yang, Z., C. Xia, S. Zhao, H. Li, Y. Peng, L. Xiang, and W. Li, “Non-blind zone MOD method based on incomplete compensation of detection coil for EV,” *Proceedings of the CSEE*, Vol. 42, No. 20, 7363–7375, 2022.
- [6] Chen, Z. and Z. Xian, “Research on improving interoperability of electric vehicle wireless power transfer based on frequency adjustment,” *Transactions of China Electrotechnical Society*, Vol. 38, No. 5, 1237–1247, 2023.
- [7] Xin, B., X. Ma, C. Cai, S. Wu, and J. Liu, “Omnidirectional wireless power transfer system for unmanned aerial vehicle based on spatial rotating magnetic field,” in *Proceedings of the CSEE*, Vol. 43, No. 12, 4769–4779, 2023.
- [8] Su, Y., L. Qian, Z. Liu, *et al.*, “Underwater electric-field coupled wireless power transfer system with rotary coupler and parameter optimization method,” *Transactions of China Electrotechnical Society*, Vol. 37, No. 10, 2399–2410, 2022.
- [9] Chen, K. Y. J., “Research on 350 kW high power wireless power transfer system for rail transit,” *Transactions of China Electrotechnical Society*, Vol. 37, No. 10, 2411–2421+2445, 2022.
- [10] Yi, J., P. Yang, Z. Li, P. Kong, and J. Li, “Mutual inductance calculation of circular coils for an arbitrary position with a finite magnetic core in wireless power transfer systems,” *IEEE Transactions on Transportation Electrification*, Vol. 9, No. 1, 1950–1959, 2023.
- [11] Li, Z., Z. Lin, P. Yang, J. Yi, and S. Huang, “Calculation of the coupling coefficient of an arbitrarily positioned circular coil for wireless power transfer system with a double-layered finite magnetic shield,” *Transactions of China Electrotechnical Society*, Vol. 37, No. 24, 6306–318, 2022.
- [12] Akyel, C., S. Babic, and S. Kincic, “New and fast procedures for calculating the mutual inductance of coaxial circular coils (circular coil-disk coil),” *IEEE Transactions on Magnetics*, Vol. 38, No. 5, 2367–2369, 2002.
- [13] Babic, S., C. Akyel, and S. J. Salon, “New procedures for calculating the mutual inductance of the system: Filamentary circular coil-massive circular solenoid,” *IEEE Transactions on Magnetics*, Vol. 39, No. 3, 1131–1134, 2003.
- [14] Babic, S. and C. Akyel, “Improvement in calculation of the self- and mutual inductance of thin-wall solenoids and disk coils,” *IEEE Transactions on Magnetics*, Vol. 36, No. 4, 1970–1975, 2000.
- [15] Conway, J. T., “Inductance calculations for circular coils of rectangular cross section and parallel axes using Bessel and Struve functions,” *IEEE Transactions on Magnetics*, Vol. 46, No. 1, 75–81, 2010.
- [16] Conway, J. T., “Inductance calculations for noncoaxial coils using Bessel functions,” *IEEE Transactions on Magnetics*, Vol. 43, No. 3, 1023–1034, 2007.
- [17] Pahlavani, M. R. A., H. A. Mohammadpour, and A. Shoulaie, “Numerical and experimental analysis of modular-toroidal-coil inductance applicable to Tokamak reactors,” *IEEE Transactions on Plasma Science*, Vol. 38, No. 2, 113–120, 2010.
- [18] Wu, D., T. He, X. Wang, and Q. Sun, “Analytical modeling and analysis of mutual inductance coupling of rectangular spiral coils in inductive power transfer,” *Transactions of China Electrotechnical Society*, Vol. 33, No. 3, 680–688, 2018.
- [19] Wu, D., Q. Sun, X. Wang, and F. Yang, “Analytical model of mutual coupling between rectangular spiral coils with lateral misalignment for wireless power applications,” *IET Power Electronics*, Vol. 11, No. 5, 781–786, 2018.
- [20] Joy, E. R., A. Dalal, and P. Kumar, “Accurate computation of mutual inductance of two air core square coils with lateral and angular misalignments in a flat planar surface,” *IEEE Transactions on Magnetics*, Vol. 50, No. 1, 1–9, 2014.
- [21] Luo, Z. and X. Wei, “Analysis of square and circular planar spiral coils in wireless power transfer system for electric vehicles,” *IEEE Transactions on Industrial Electronics*, Vol. 65, No. 1, 331–341, 2018.
- [22] Kushwaha, B. K., G. Rituraj, and P. Kumar, “3-D analytical model for computation of mutual inductance for different misalignments with shielding in wireless power transfer system,” *IEEE Transactions on Transportation Electrification*, Vol. 3, No. 2, 332–342, 2017.
- [23] Luo, Z., S. Nie, M. Pathmanathan, W. Han, and P. W. Lehn, “3-D analytical model of bipolar coils with multiple finite magnetic shields for wireless electric vehicle charging systems,” *IEEE Transactions on Industrial Electronics*, Vol. 69, No. 8, 8231–8242, 2022.
- [24] Kushwaha, B. K., G. Rituraj, and P. Kumar, “A subdomain analytical model of coil system with magnetic shields of finite dimensions and finite permeability for wireless power transfer systems,” *IEEE Transactions on Magnetics*, Vol. 56, No. 12, 1–11, 2020.